Research Article | Vol. 12, No. 12 / 1 Dec 2022 / Optical Materials Express 4594
Optical Materials EXPRESS

Thermally switchable, bifunctional, scalable, mid-infrared metasurfaces with VO_2 grids capable of versatile polarization manipulation and asymmetric transmission

ANDRIY E. SEREBRYANNIKOV,[1,4,*] AKHLESH LAKHTAKIA,[2] AND EKMEL OZBAY[3]

[1]*Division of Physics of Nanostructures, ISQI, Faculty of Physics, Adam Mickiewicz University, 61-614 Poznań, Poland*
[2]*Department of Engineering Science and Mechanics, The Pennsylvania State University, University Park, Pennsylvania 16802, USA*
[3]*Nanotechnology Research Center (NANOTAM), National Institute of Materials Science and Nanotechnology (UNAM), Department of Physics, Department of Electrical Engineering, Bilkent University, 06800 Ankara, Turkey*
[4]*andser@amu.edu.pl*
[*]*aeserebr@googlemail.com*

Abstract: We conceptualized three-array scalable bifunctional metasurfaces comprising only three thin strip grids and numerically determined their characteristics in the mid-infrared spectral regime for switchable operation scenarios involving polarization manipulation and related diodelike asymmetric transmission (AT) as one of two functionalities. A few or all of the grids were taken to be made of VO_2, a bifunctionality-enabling phase-change material; there are no layers and/or meta-atoms comprising simultaneously both metal and VO_2. For each proposed metasurface, two effective structures and, therefore, two different functionalities exist, corresponding to the metallic and insulating phases of VO_2. The achieved scenarios of functionality switching significantly depend on the way in which VO_2 is incorporated into the metasurface. Switchable bands of polarization manipulation are up to 40 THz wide. The AT band can be modulated when Fabry–Perot (anti-) resonances come into play. Besides, transmission regimes with the cross-polarized component insensitive to VO_2 phase change are possible, as well as the ones with all co- and cross-polarized components having the same magnitude for both linear polarizations of the incident wave.

1. Introduction

Polarization manipulation and related asymmetric transmission (AT) achievable *via* quasiplanar metamaterials constitute a topic of considerable attention from the mid-2000's. Most researchers were initially focused on few-layer metasurfaces comprising coupled periodic arrays of (complementary) subwavelength resonators [1–5]. Later, structures with a central resonator/meta-atom array and two outer grids, which are capable of wideband AT, were proposed [6–8]. Moreover, geometric-phase gradient metasurfaces having high potential for polarization control should be mentioned [9,10]. Besides, metasurfaces and heterostructures enabling efficient manipulation by orbital angular momentum have been suggested [11]. Notably, a single-array structure can deliver polarization manipulation/conversion with AT for incident circularly polarized (CP) plane waves, but at least two coupled arrays are needed for AT when the incident plane wave is linearly polarized (LP).

Mid-infrared (MIR) and near-infrared applications need rather simple (e.g., resonator-free) design solutions suitable for avoiding absorption enhancement, assuring AT capability as well as

#465468 https://doi.org/10.1364/OME.465468
Journal © 2022 Received 5 Jul 2022; revised 18 Oct 2022; accepted 31 Oct 2022; published 16 Nov 2022

Optical Materials EXPRESS

facile fabrication, for instance, by using lithography to create topographic substrates [12–14] over which dielectric materials and/or metals are deposited using standard physical and/or chemical vapor deposition techniques [15,16]. In particular, polarization-converting, few-layer, anisotropic structures comprising grids and related components (but not resonators and meta-atoms) have been fabricated and experimentally studied for different parts of electromagnetic spectrum including the near-infrared and visible spectral regimes [17–19]. Such structures are often considered to be dispersionless and, therefore, promising for applications.

The research landscape for polarization control changed dramatically when tunable materials were introduced to metasurfaces and metamaterials, thereby enabling reconfigurable and multifunctional devices [20–23]. Magnetically, electrically, thermally, and optically tunable materials such as graphene, InAs, InSb, GeTe, CdTe, VO_2, and ITO are often considered, in this context. Transition from an insulator (i) phase to a metallic (m) phase, and/or *vice versa*, mediated by a control parameter may occur for many natural materials [24]. In particular, VO_2 is a thermally tunable phase-change material useful from the terahertz (THz) to the visible spectral regimes [25–28]. It displays a hysteretic insulator-metal-insulator double transition [29,30]. This transition is due to the change of crystallographic phase from monoclinic to tetragonal that occurs as temperature T is raised from a value slightly lower than 58 °C to a value slightly above 72 °C [31], and this transition is reversible on cooling. As a result, VO_2 behaves as a dissipative insulator (i-VO_2) when monoclinic and metallic (m-VO_2) when tetragonal, provided the free-space wavelength $\lambda \gtrsim 1100$ nm [32].

The tuning and switching capabilities acquired by metasurfaces due to phase-change materials are often considered in the context of multifunctional operation [33]. Indeed, changing the material phase may lead not only to on-off switching of a certain functionality, but also may enable two or more functionalities for either a fixed frequency or closely spaced frequencies. The simplest form in which VO_2 has been used in photonic heterostructures and metasurfaces is as thin homogeneous layers [34–37], but the variety of functionality-switching scenarios then is limited. VO_2 pads/inserts have been incorporated in metallic subwavelength resonators for THz applications, especially for switchable polarization manipulation and AT [38–41]. In this case, both a metal and VO_2 are present in one meta-atom. Also, a metal and VO_2 have been jointly used in a functional array-based single layer [42] or bilayer [43]. However, the feasibility of such meta-atoms and other hybrid components for MIR applications is not obvious. Meta-atoms comprising only VO_2 or another thermally tunable material have also been proposed to exploit resonances in m-VO_2 and/or i-VO_2 phase [44–49]. Patterned thin films of a phase-change material have been utilized either to directly enable tunability or indirectly tune a functionality enabled by other components [50–55]. Switchable devices based on phase-change materials are preferred because the constitutive contrast in the two phases is large and fabrication is straightforward, even though they typically consume more energy and the switching speed is low in comparison to all-optical devices exploiting the optical Kerr effect or generation of free carriers [56,57].

In this paper, we conceptualize and numerically justify the potential of three-array metasurfaces comprising *only* VO_2 grids and Ag grids, which are capable of temperature-dependent bifunctional operation in the MIR regime that includes thermally switchable wideband polarization manipulation and related diodelike AT for LP plane waves. The motivation for this study includes avoidance of subwavelength resonators (made of either a metal or a phase-change material, or both) to prevent possible resonance enhancement of absorption. Our specific aims within this study are to: (a) demonstrate the role of VO_2 grids as enablers of specific functionality-switching scenarios involving polarization conversion and AT for one of VO_2 phases; (b) clarify how the manner of using VO_2 in the grids determines which of the bifunctional operating scenarios are achievable, by comparing three different schemes for incorporating VO_2; (c) demonstrate scalability of the proposed designs in the MIR regime for wider applicability; (d) show that conduction in m-VO_2 is sufficiently large and dissipation is sufficiently small to replace a metal

Optical Materials EXPRESS

in either some or all grids, and conserve high capability of polarization manipulation; and (e) clarify the emergence and role of Fabry–Perot resonances in the resulting functionality and scalability. Geometrically, the studied structures may remind of those proposed by others in Refs. [17] and [19], in contrast to which a phase-change tunable material is used by us as the bifunctionality-enabling material. One of three schemes used here is geometrically similar to the one proposed in Ref. [55] but for another frequency range (far-infrared) while using graphene, an electrically tunable material. Since the required thickness of VO_2 strips ranges only from 40 to 180 nm and m-VO_2 is not such a good conductor as either copper or silver, the capability of the structures comprising VO_2 grids for polarization manipulation is not evident at first glance and needs to be established soundly. The studied metasurfaces are feasible and require standard fabrication techniques. For demonstration purposes, consideration of such a geometrically classic configuration is sufficient. Maximization of AT contrast and/or ON–OFF switching contrast is beyond the scope of this paper, as well as comparison with metsaurfaces containing other thermally, electrically or magnetically tunable materials.

We note that pure VO_2 can be challenging to deposit because of the commonplace formation of non-stochiometric vanadium oxide (i.e., VO_ζ, where ζ is not the ratio of two small integers) [58,59] whose thermal-tunability characteristics can differ very significantly from those of stochiometric forms (such as VO_2, V_2O_3, V_2O_5, V_4O_7, etc.). However, the metal-insulator and insulator-metal transitions still persist [60] and our design considerations will still hold.

2. Results and discussion

Metasurfaces of three types are considered, differing in the way in which VO_2 is used. Every metasurface was assumed to be illuminated by a normally incident LP plane wave. CST Studio Suite [61] was used to calculate the complex-valued transmission coefficients τ_{nm}^M and τ_{nm}^I, where the subscripts $m \in \{x, y\}$ and $n \in \{x, y\}$, respectively, identify the direction of the electric field of the incident LP plane wave and the direction of the transmitted electric field in the far zone. Front-face and back-face illuminations correspond to the propagation of the incident plane wave along the $-z$ and $+z$ directions, respectively. These cases are identified by the superscripts $\rightarrow$ and $\leftarrow$. The considered structure is Lorentz reciprocal [62], so $|\tau_{yy}^{\rightarrow}| = |\tau_{yy}^{\leftarrow}|$, $|\tau_{xx}^{\rightarrow}| = |\tau_{xx}^{\leftarrow}|$, $|\tau_{xy}^{\rightarrow}| = |\tau_{yx}^{\leftarrow}|$, and $|\tau_{yx}^{\rightarrow}| = |\tau_{xy}^{\leftarrow}|$. Asymmetry in transmission may be desirably strong when either (a) $|\tau_{xy}^{\rightarrow}| \gg |\tau_{xy}^{\leftarrow}|$ and $|\tau_{xy}^{\rightarrow}| \gg |\tau_{xx}^{\rightarrow}|$, or (b) $|\tau_{xy}^{\rightarrow}| \ll |\tau_{xy}^{\leftarrow}|$ and $|\tau_{xx}^{\leftarrow}| \ll |\tau_{xy}^{\leftarrow}|$. For the purposes of numerical study, the complex relative permittivity of VO_2 in the [34.5, 80] THz frequency range was calculated from experimental data [Ref. [63], Fig. 2(c)] and then extrapolated down to 30 THz frequency. The Drude model of the complex relative permittivity of Ag was used, i.e., $\varepsilon_r^{Ag}(\omega) = 1 - \left(\omega_p^{Ag}\right)^2 / [\omega(\omega + i\gamma)]$, where $\omega = 2\pi f$ is the angular frequency and f is the linear frequency, the angular plasma frequency $\omega_p^{Ag} = 1.37 \times 10^{16}$ rad s^{-1}, and the collision frequency is $\gamma = 2.73 \times 10^{13}$ rad s^{-1} [64].

2.1. Case of the central grid made of VO_2

First, we consider the metasurfaces 1A–1F, each with a VO_2 grid separated from two Ag grids by dielectric spacers with the central grid oriented at 45° in the transverse plane with respect to the other two grids, as shown in Fig. 1(a). Thus, each metasurface has two conducting grids for i-VO_2 and effectively three conducting grids for m-VO_2. The central grid works like a phase screen for i-VO_2, as we have recently shown [54]. The different electromagnetic properties of this grid pre-determine the possibility of bifunctional operation which includes here (i) transmission with the dominant cross-polarized components and AT for m-VO_2 and (ii) reflection for i-VO_2. Graphs of the transmission-coefficient magnitudes vs. f are presented for all six metasurfaces in Figs. 1(b)–(g).

Optical Materials EXPRESS

Let

$$\psi = |\tau_{yx}^{M\rightarrow}|^2/|\tau_{xx}^{M\rightarrow}|^2 \tag{1}$$

and

$$\zeta = (|\tau_{yx}^{M\rightarrow}|^2 + |\tau_{xx}^{M\rightarrow}|^2)/(|\tau_{yx}^{I\rightarrow}|^2 + |\tau_{xx}^{I\rightarrow}|^2). \tag{2}$$

The quantities ψ and ζ indicate, respectively, the strength of polarization conversion in transmission and metal-phase-to-insulator-phase transmittance contrast. Switchable AT appears, for instance, at $f = 64$ THz in Fig. 1(b) for metasurface 1A, where $\psi = 87$ and $\zeta = 8.2$, and at $f = 37$ THz in Fig. 1(e) for metasurface 1D, where $\psi = 147$ and $\zeta = 10$. Similar transmission features are observed in Figs. 1(b)–(d) for metasurfaces 1A–1C as in Figs. 1(e)–(g) for metasurfaces 1D–1F, the spacers in the first three metasurfaces being two-thirds in thickness compared to those in the last three metasurfaces.

The transmission features are *scalable*, albeit approximately, when the scaling coefficient, s, is varied, as occurs for metasurfaces 1A, 1B, and 1C, as well as for metasurfaces 1D, 1E, and 1F. They are downshifted and compressed in the f-domain when s is increased. This scaling can be quantified by comparing the spectral locations of the typical minimums and maximums. For instance, the minimum of $|\tau_{yx}^{M\rightarrow}|$ occurs at 65 THz for 1D [Fig. 1(e)], 53 THz for 1E [Fig. 1(f)], and 38 THz for 1F [Fig. 1(g)], in inverse proportion to the value of s.

In contrast with conventional Fabry–Perot anti-resonances which appear for a homogeneous dielectric slab, the minimums of $|\tau_{yx}^{M\rightarrow}|$ in Figs. 1(b)–(g) correspond to the condition

$$2\varepsilon_{sp}^{1/2}kt \approx \ell\pi, \tag{3}$$

where ε_{sp} is the relative permittivity of the spacer, $k = 2\pi/\lambda$ is the free-space wavenumber, and $\ell \in \{2, 4\}$. These minimums, identified by *FP* in the graphs, have nearly the same spectral locations as a part of the maximums in the case of a homogeneous dielectric slab of thickness $2t$. Similarly, Fabry-Perot anti-resonances are spectrally shifted when only spacer thickness, $2t$, is varied, as observed from the comparison of metasurfaces 1A and 1D, 1B and 1E, and 1C and 1F. Notably, most of the energy of the incident plane wave is reflected at the minimums of $|\tau_{yx}^{M\rightarrow}|$, while reflections are weak at the maximums of $|\tau_{yx}^{M\rightarrow}|$. By adjusting the spacer thickness, we can obtain on-off switchable, diodelike AT with a desired bandwidth.

Incidentally, $|\tau_{yx}^{\rightarrow}|$ can be insensitive to the crystallographic phase of VO_2, as occurs in the vicinity of 80 THz in Fig. 1(d) for metasurface 1C. On the other hand, different maximums of $|\tau_{yx}^{M\rightarrow}|$ show different sensitivity to the crystallographic phase of VO_2. For instance, in Fig. 1(g) for metasurface 1F, $\zeta \approx 10$ at 47 THz but $\zeta \approx 2$ at 62 THz. Notably, metasurfaces 1A-1F are geometrically similar to the electrically tunable metasurface with two metallic and one graphene grid proposed in Ref. [55] for the far-infrared spectral regime.

2.2. Case of the outer grids made of VO_2

Next, let us swap Ag and VO_2 in metasurfaces 1A–1F to form metasurfaces 2A–2F, each with an Ag grid separated from two VO_2 grids by dielectric spacers, as shown in Fig. 2(a). In this case, each metasurface has one conducting grid for i-VO_2 and effectively three conducting grids for m-VO_2. The front-face and the back-face grids work like a phase screen for i-VO_2 [54]. Hence, the type of bifunctionality is pre-determined here by the switchable electromagnetic properties of the outer grids, so it includes (i) transmission with the dominant cross-polarized components and AT for m-VO_2 and (ii) modification of the polarization type for the transmitted wave for i-VO_2. For m-VO_2, the cross-polarized component of the transmitted plane wave is dominant compared to the co-polarized one, i.e., ψ>10. In particular, $\psi = 11.7$ at 50 THz in Fig. 2(b) for 2A, 19.7 at 30 THz in Fig. 2(c) for 2B, and 28.4 at 62 THz in Fig. 2(g) for 2F. For i-VO_2, none of the transmission components is suppressed, i.e., they all are of the same order of magnitude. Thus,

Optical Materials EXPRESS

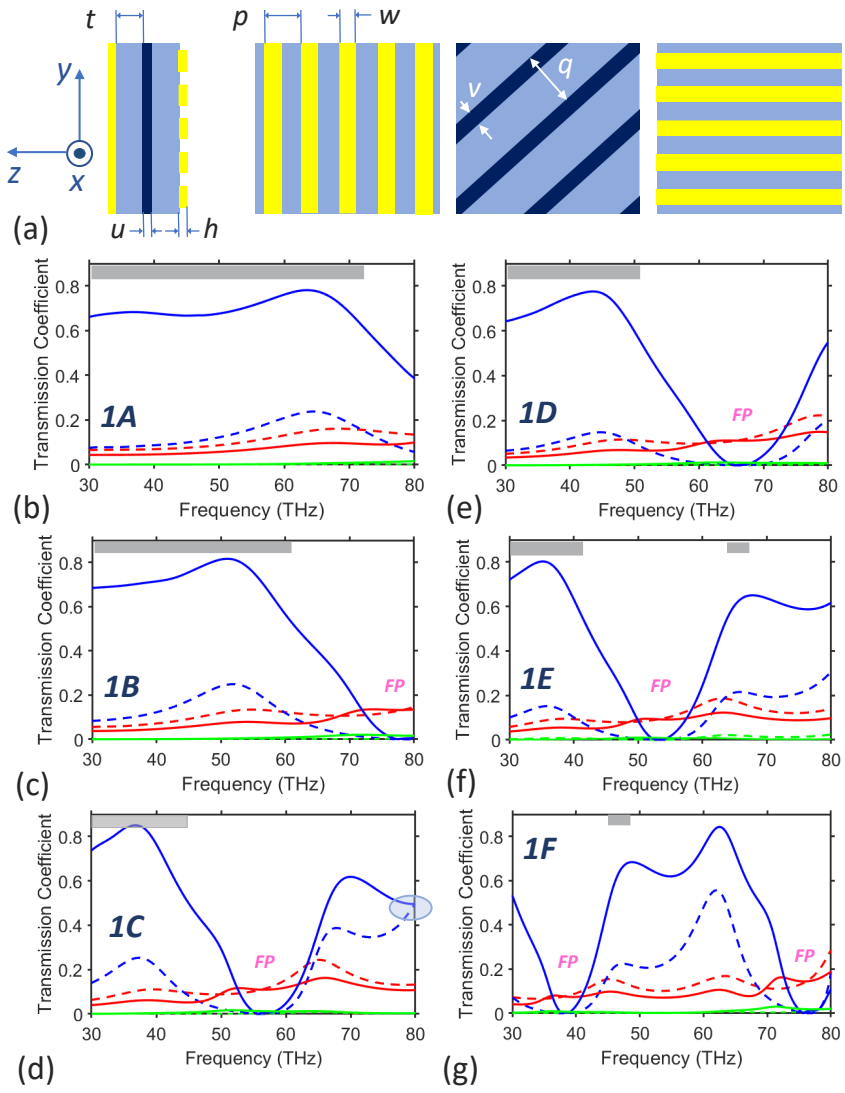

Fig. 1. Geometry and transmission vs frequency for six metasurfaces labeled 1A –1F. (a) From left to right: side cross-section view, front view, mid cross-section view, and back view; each metasurface comprises a VO_2 grid (shown in dark blue) separated from two outer silver grids (yellow) by dielectric spacers (light blue); the central grid is oriented at 45° with respect to the other two grids in the xy plane. Spectrums of transmission-coefficient magnitudes for spacer thickness (b, c, d) $t = 1000s$ nm and (e, f, g) $t = 1500s$ nm, $h = 50s$ nm, and $p = 600s$ nm with scaling coefficient (b,e) $s = 1$, (c,f) $s = 1.25$, and (d,g) $s = 1.75$; $w = p/2$, $q = \sqrt{2}p$, $u = 2h$, $v = w$; relative permittivity of spacer $\varepsilon_{sp} = 2.1$. Solid blue lines: $|\tau_{yx}^{M\rightarrow}|$; solid green lines: $|\tau_{xy}^{M\rightarrow}|$; solid red lines: $|\tau_{xx}^{M}| = |\tau_{yy}^{M}|$; dashed blue lines: $|\tau_{yx}^{I\rightarrow}|$; dashed green lines: $|\tau_{xy}^{I\rightarrow}|$; dashed red lines: $|\tau_{xx}^{I}| = |\tau_{yy}^{I}|$. Grey rectangles indicate the frequency ranges which can be used for ON–OFF switching of AT. Bluish ellipse indicates the case when $|\tau_{yx}^{I\rightarrow}| \approx |\tau_{yx}^{M\rightarrow}| > 0.4$.

Optical Materials EXPRESS

transmission mode is conserved when the crystallographic phase of VO_2 is thermally altered in 2A–2F, this characteristic being absent in Fig. 1 for 1A–1F. Moreover, spectral regimes exist in which co- and cross-polarized transmission channels contain *equal energy*, regardless of whether the front face or the back face is illuminated. That is evident, for instance, at $f = 80$ THz in Fig. 2(c) for the metasurface 2B and at $f = 55$ THz in Fig. 2(f) for the metasurface 2E.

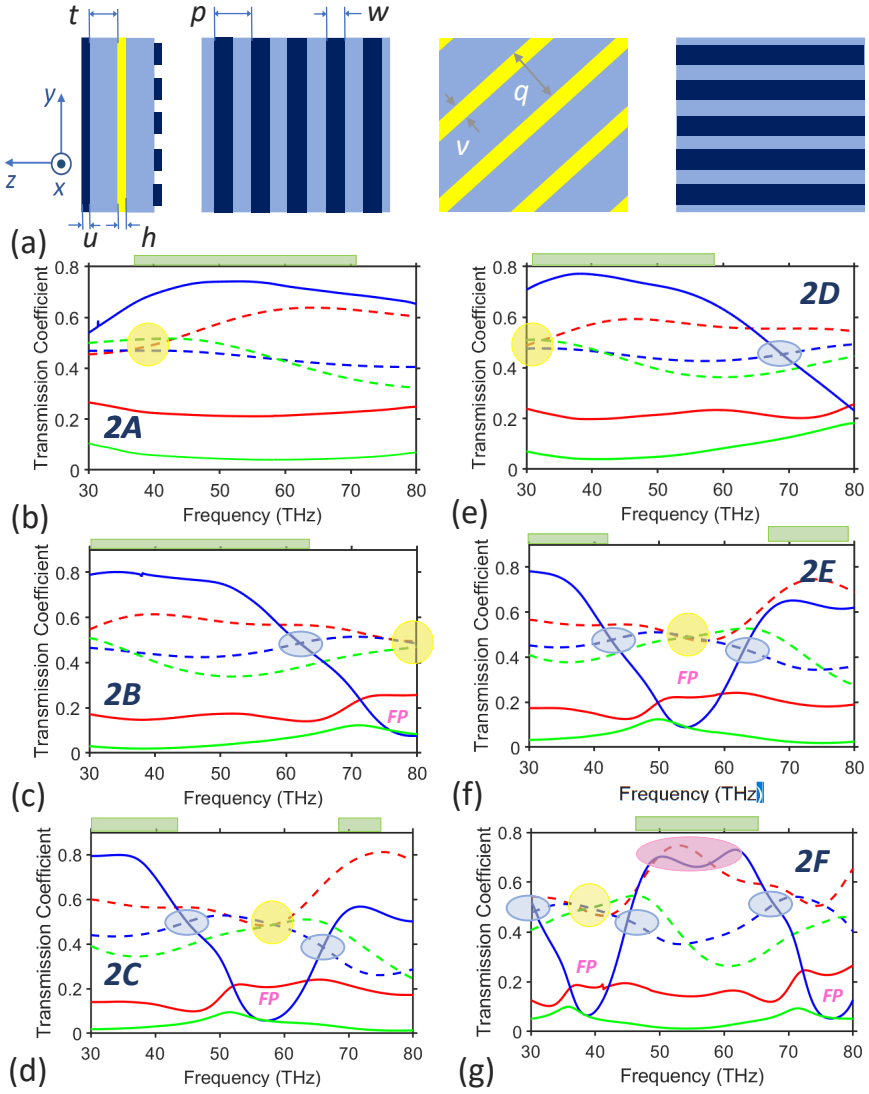

Fig. 2. Same as Fig. 1 but for metasurfaces labeled 2A–2F, each comprising an Ag grid (shown in yellow) separated from VO_2 grids (dark blue) by dielectric spacers (light blue). Scaling coefficient (b,e) $s = 0.75$, (c,f) $s = 1.25$, and (d,g) $s = 1.75$. Light green rectangles in each plot indicate the f-ranges which may be suitable for AT when m-VO_2 is used. Yellowish circles indicate spectral regimes with $|\tau_{yx}^{I\rightarrow}| \approx |\tau_{xx}^{I\rightleftharpoons}| \approx |\tau_{xy}^{I\rightarrow}| \approx |\tau_{yy}^{I\rightleftharpoons}|$. Rosy ellipse indicates the regime of $|\tau_{yx}^{M\rightarrow}| \approx |\tau_{xx}^{I}|$.

The features observed in Figs. 2(e)–(g) are similar to the ones in Figs. 2(b)–(d); so that a desired modulation of the transmission spectrum can be obtained by varying t to affect Fabry–Perot resonances and anti-resonances, as well as a desired location of the AT band for m-VO_2 and the

Optical Materials EXPRESS

equal-energy regime for i-VO_2. These bands may coincide or not coincide, depending on which functionality-switching scenario is needed. Scaling manifests itself in Fig. 2, similarly to Fig. 1, in the redshift of transmission features with increase of the scaling coefficient s. In addition, transmission spectrum becomes more compressed when a thicker spacer is used.

Despite the structures and functional capabilities of the metasurfaces 2A–2F being different from those of the metasurfaces 1A–1F, the insensitivity of the latter to the crystallographic phase of VO_2 is also exhibited by the former for specific spectral regimes and field components. This is exemplified by $|\tau_{yx}^{\rightarrow}|$, e.g., at $f = 62$ THz in Fig. 2(c) for 2B and 43 THz as well as 63 THz in Fig. 2(f) for 2E. The number of the related spectral regimes, in which the insensitivity is observed within the considered f-range, increases with t, since the transmission spectrum thereby becomes more compressed as the spacer thickens. Among the switching regimes achievable with 2A–2F, the one observed in Fig. 2(g) for $f \in [45, 60]$ THz should be mentioned. Here, the strongest transmission component has nearly the same magnitude, but represents either the co- or the cross-polarized component for the same incident plane wave, depending on whether i-VO_2 or m-VO_2 is used.

For i-VO_2, the metasurfaces 2A–2F can efficiently transmit an incident LP plane wave as a plane wave whose polarization state is close to being circular. We have adopted the usual optics convention: an LCP (left-handed CP) wave satisfies the condition $\nabla \times \vec{E} = k\vec{E}$, whereas an RCP (right-handed CP) wave satisfies the condition $\nabla \times \vec{E} = -k\vec{E}$. Figure 3 presents transmission results for metasurfaces 2C and 2F, but the transmission is quantified now for CP outgoing waves. As observed in Fig. 3, both $|\tau_{Rx}^{\rightarrow}|/|\tau_{Lx}^{\rightarrow}|>1$ and $|\tau_{Ry}^{\rightarrow}|/|\tau_{Ly}^{\rightarrow}|>1$ for both selected metasurfaces. Moreover, spectral regimes exist in which $|\tau_{Rx}^{\rightarrow}|/|\tau_{Lx}^{\rightarrow}|>5$ and/or $|\tau_{Ry}^{\rightarrow}|/|\tau_{Ly}^{\rightarrow}|>5$, so that linear-to-(nearly-)circular polarization conversion (LCPC) takes place. The selective coupling of the incident LP waves to the outgoing CP waves allows the AT ranges for m-VO_2 and LCPC ranges for i-VO_2 to overlap when s and t are properly adjusted. In this case, a change of crystallographic phase of VO_2 results in bifunctional operation at fixed f. Otherwise, bifunctionality is obtained while using different f-ranges for the two crystallographic phases of VO_2. To compare, the metasurfaces 2A–2F for i-VO_2 work similarly to the ones proposed in Ref. [42] for the far-infrared spectral regime. However, in our case the functionality-switching scenario is different, because the capability of transmission is conserved for both m-VO_2 and i-VO_2 due to the design specifics. Notably, the metasurfaces 1A–1F do not show a capability for linear-to-(nearly-)circular polarization conversion.

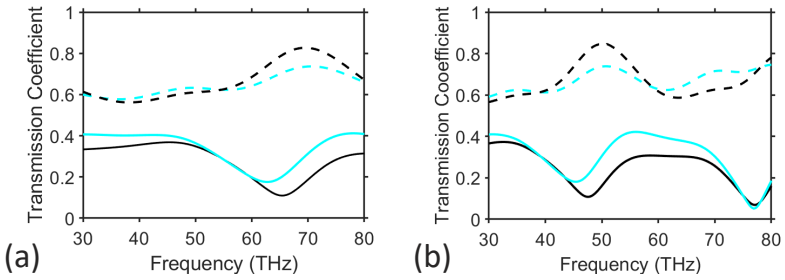

Fig. 3. Linear-to-(nearly-)circular polarization conversion for metasurfaces (a) 2C and (b) 2F. Dashed cyan lines: $|\tau_{Rx}^{\rightarrow}|$, solid cyan lines: $|\tau_{Lx}^{\rightarrow}|$, dashed black lines: $|\tau_{Ry}^{\rightarrow}|$, and solid black lines: $|\tau_{Ly}^{\rightarrow}|$.

2.3. Case of a metal-free structure

Finally, we consider the case of metal-free metasurfaces, i.e., when all three grids are made of VO_2. As a result, every metasurface in Fig. 4 has effectively three conducting grids for m-VO_2

Optical Materials EXPRESS

but comprises only insulators for i-VO_2. Now, we intend to obtain the co-polarized, weakly attenuated and weakly sensitive to variations in f transmission for one of the VO_2 phases and keep the capability of polarization manipulation and related AT for the other. This is why we want to abandon metals here. This scenario of functionality switching is totally different as compared to the ones in Figs. 1 and 2. The results are presented in Figs. 4(b)–(e) for the same geometric parameters as for Figs. 1(b), (c), (d), and (g).

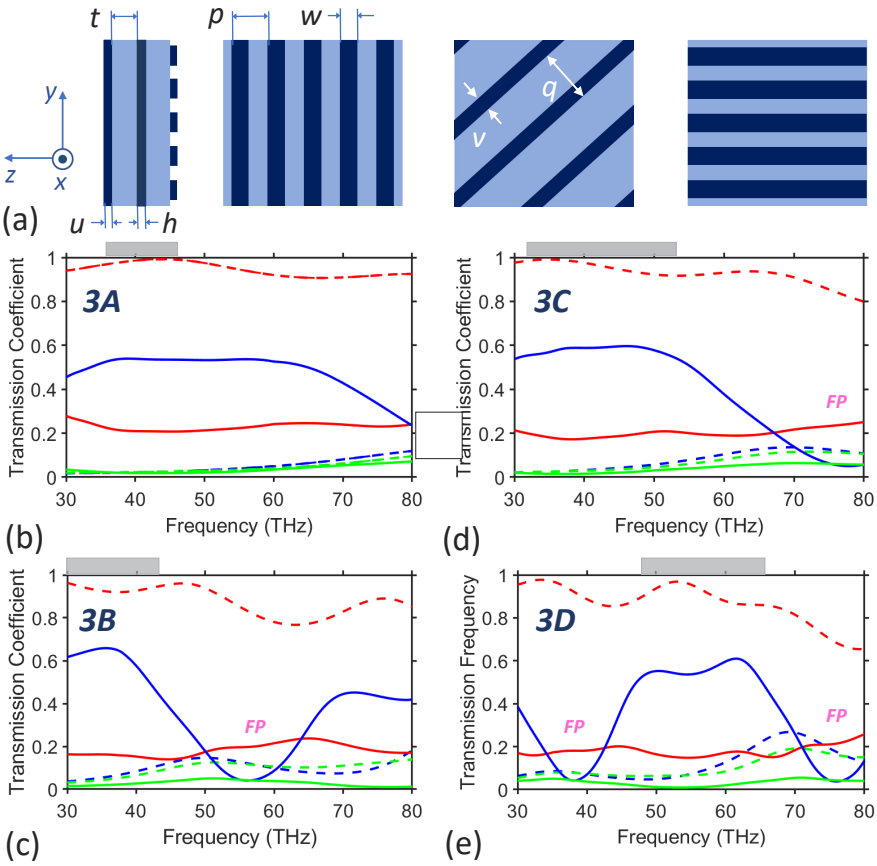

Fig. 4. Spectrums of transmission-coefficient magnitudes calculated for four metasurfaces, labeled 3A-3D, each comprising three VO_2 grids (shown in dark blue) separated by dielectric spacers (light blue). (a) From left to right: side cross-section view, front view, mid cross-section view, and back view, respectively. (b)–(e) Transmission spectrums for spacer thickness (b, c, d) $t = 1000s$ nm and (e) $t = 1500s$ nm. Scaling coefficient (b) $s = 0.75$, (c) $s = 1.25$ and (d,e) $s = 1.75$. See Fig. 1 for other details.

The value of ψ in Fig. 4 typically does not exceed 10. For instance, $\psi = 6.5$ at 38 THz in Fig. 4(b) for metasurface 3A, $\psi = 7$ at 38 THz in Fig. 4(c) for 3B, and $\psi = 12$ at 62 THz in Fig. 4(e) for 3D. Along with the achievable magnitude of $|\tau_{yx}^{M\rightarrow}|$, this result is quite good since the metasurfaces do not contain any metal or cylindrical or other volume dielectric resonators (in contrast, say, with Ref. [46]). Also for these metasurfaces we obtain scaling as the redshift of the basic transmission features occurring with increase of s, as observed from a comparison of Figs. 4(b), 4(c) and 4(d), in spite of VO_2 being dispersive. Notably, the shifts of the minimums of $|\tau_{yx}^{M\rightarrow}|$ and the edges of the strong-transmission ranges occur due to change of either s or t, so these parameters provide two degrees of freedom for designing the transmission spectrum. The

Optical Materials EXPRESS

various types of bifunctional operation scenarios that are achieved by changing VO_2 phase are summarized in Table 1.

Table 1. Comparison of designed metasurfaces in terms of the basic functionalities of bifunctional operation scenarios

Metasurface	Metallic phase of VO_2	Insulator phase of VO_2
1A–1F	high-efficiency linear-to-linear polarization conversion in transmission mode	reflection without polarization conversion
2A–2F	high-efficiency linear-to-linear polarization conversion in transmission mode	linear-to-(nearly-)circular polarization conversion in transmission mode
3A–3D	moderate-efficiency linear-to-linear polarization conversion in transmission mode	high-efficiency transmission without polarization conversion

A detailed investigation of the robustness of the performance characteristics of the few-array metasurfaces presented in Figs. 1–4 is outside the scope of this paper. However, spot checks revealed that the performances are not adversely affected, apart from slight spectral shifts and slight changes in the magnitudes of co- and cross-polarized transmission coefficients, even when geometric dimensions of the grids are altered by ±10%.

3. Conclusion

To summarize, we studied transmission through few-array metasurfaces comprising only three strip grids and exhibiting switchable polarization manipulation and related AT for LP incident plane waves in the 30–80-THz frequency range. The proposed structures are approximately scalable within this spectral regime. Subwavelength resonators, inserts, and pads are not needed, thereby reducing fabrication complexities for MIR devices. Moreover, the absence of resonators can prevent resonance absorption enhancement. Diverse bifunctional operating scenarios can be achieved, depending on whether VO_2 is used as the material of only the two outer, only the central, or all three grids. In all scenarios, well-pronounced AT connected with polarization manipulation occurs for m-VO_2. It is switched for another functionality when m-VO_2 is changed for i-VO_2. This is true also when all three grids are made of VO_2, i.e., the metasurface is metal-free. Fabry–Perot (anti-)resonances manifest themselves in a way different from the case of a homogeneous dielectric slab of nearly the same thickness as two spacers in the studied structures and enable efficient modulation of the polarization effects and transmission. The observed capability for polarization manipulation and AT remains while adding a semi-infinite dielectric substrate at the back side (results are not shown). The variety of the polarization manipulation regimes includes also the ones with cross-polarized transmission insensitive to the change of m-VO_2 to i-VO_2, or vice versa. Moreover, all transmission components may have the same magnitudes, regardless of whether it is co- or cross-polarized and which of two linear polarizations is attributed to the incident LP wave. Besides the studied metasurfaces, those with only the front-face grid made of VO_2 were examined (results are not shown). The transmission efficiency can be further increased by using wider strips of the central grid than in the presented examples. For instance, $|\tau_{yx}^{M\rightarrow}| \approx 0.8$ and 0.7 were obtained in the AT bands for the metasurfaces similar to 1F and 3D, respectively. All discussed features are quite universal and can occur for a rather wide range of spacer's relative permittivity, although a lower relative permittivity can often be preferred.

Funding. Narodowe Centrum Nauki (UMO-2020/39/I/ST3/02413).

Acknowledgments. A. L. thanks the Charles Godfrey Binder Endowment at The Pennsylvania State University for ongoing support. E. O. thanks the Turkish Academy of Sciences for partial support.

Disclosures. The authors declare that there are no conflicts of interest related to this article.

Optical Materials EXPRESS

Data Availability. Data underlying the results presented in this paper are not publicly available at this time but may be obtained from the corresponding author upon reasonable request.

References

1. C. Menzel, C. Helgert, C. Rockstuhl, E.-B. Kley, A. Tünnermann, T. Pertsch, and F. Lederer, "Asymmetric transmission of linearly polarized light at optical metamaterials," Phys. Rev. Lett. **104**(25), 253902 (2010).
2. M. Mutlu, S. Cakmakyapan, A. E. Serebryannikov, and E. Ozbay, "One-way reciprocal spoof surface plasmons and relevant reversible diodelike beaming," Phys. Rev. B **87**(20), 205123 (2013).
3. V. A. Fedotov, P. L. Mladyonov, S. L. Prosvirnin, A. V. Rogacheva, Y. Chen, and N. I. Zheludev, "Asymmetric propagation of electromagnetic waves through a planar chiral structure," Phys. Rev. Lett. **97**(16), 167401 (2006).
4. C. Huang, Y. Feng, J. Zhao, Z. Wang, and T. Jiang, "Asymmetric electromagnetic wave transmission of linear polarization via polarization conversion through chiral metamaterial structures," Phys. Rev. B **85**(19), 195131 (2012).
5. Y. Cheng, J. Fan, H. Luo, F. Chen, N. Feng, X. Mao, and R. Gong, "Dual-band and high-efficiency circular polarization conversion via asymmetric transmission with anisotropic metamaterial in the terahertz region," Opt. Mater. Express **9**(3), 1365–1376 (2019).
6. D.-j. Liu, Z.-y. Xiao, X.-I. Ma, and Z.-h. Wang, "Broadband asymmetric transmission and multi-band 90° polarization rotator of linearly polarized wave based on multi-layered metamaterial," Opt. Commun. **354**, 272–276 (2015).
7. D. Liu, M. Li, X. Zhai, L. Yao, and J. Dong, "Enhanced asymmetric transmission due to Fabry-Perot-like cavity," Opt. Express **22**(10), 11707–11712 (2014).
8. J.-S. Li and F.-Q. Bai, "Dual-band terahertz polarization converter with high-efficiency asymmetric transmission," Opt. Mater. Express **10**(8), 1853–1861 (2020).
9. J. P. Balthasar Mueller, N. A. Rubin, R. C. Devlin, B. Groever, and F. Capasso, "Metasurface polarization optics: Independent phase control of arbitrary orthogonal states of polarization," Phys. Rev. Lett. **118**(11), 113901 (2017).
10. W. Luo, S. Sun, H.-X. Xu, Q. He, and L. Zhou, "Transmissive ultrathin Pancharatnam-Berry metasurfaces with nearly 100% efficiency," Phys. Rev. Appl. **7**(4), 044033 (2017).
11. K. Zhang, Y. Yuan, X. Ding, H. Li, B. Ratni, Q. Wu, J. Liu, S. Burokur, and J. Tan, "Polarization-engineered noninterleaved metasurface for integer and fractional orbital angular momentum multiplexing," Laser Photonics Rev. **15**(1), 2000351 (2021).
12. M. W. Horn, M. D. Pickett, R. Messier, and A. Lakhtakia, "Blending of nanoscale and microscale in uniform large-area sculptured thin-film architectures," Nanotechnology **15**(3), 303–310 (2004).
13. E. D. Walsby, M. Arnold, Q.-h. Wu, I. J. Hodgkinson, and R. J. Blaikie, "Growth and characterisation of birefringent films on textured silicon substrates," Microelectron. Eng. **78-79**, 436–441 (2005).
14. C. Patzig, J. Zajadacz, K. Zimmer, R. Fechner, C. Khare, and B. Rauschenbach, "Patterning concept for sculptured nanostructures with arbitrary periods," Appl. Phys. Lett. **95**(10), 103107 (2009).
15. R. J. Martín-Palma and A. Lakhtakia, "Vapor deposition techniques," in: A. Lakhtakia and R. J. Martín-Palma eds., *Engineered Biomimicry*, pp. 383–398 (Elsevier, 2013).
16. A. Sarangan, *Nanofabrication: Principles to Laboratory Practice* (CRC Press, 2019).
17. C. Pfeiffer, C. Zhang, V. Ray, L. J. Guo, and A. Grbic, "High performance bianisotropic metasurfaces: asymmetric transmission of light," Phys. Rev. Lett. **113**(2), 023902 (2014).
18. Y. Zhao, M. A. Belkin, and A. Alù, "Twisted optical metamaterials for planarized ultrathin broadband circular polarizers," Nat. Commun. **3**(1), 870 (2012).
19. C. Zhang, C. Pfeiffer, T. Jang, V. Ray, M. Junda, P. Uprety, N. Podraza, A. Grbic, and L. J. Guo, "Breaking Malus'law: highly efficient, broadband, and angular robust asymmetric light transmitting metasurface," Laser Photonics Rev. **10**(5), 791–798 (2016).
20. Q. Wang, E. T. F. Rogers, B. Gholipour, C.-M. Wang, G. Yuan, J. Teng, and N. I. Zheludev, "Optically reconfigurable metasurfaces and photonic devices based on phase change materials," Nat. Photonics **10**(1), 60–65 (2016).
21. E. Maguid, I. Yulevich, M. Yannai, V. Kleiner, M. L. Brongersma, and E. Hasman, "Multifunctional interleaved geometric-phase dielectric metasurfaces," Light: Sci. Appl. **6**(8), e17027 (2017).
22. P. Kumar, A. Lakhtakia, and P. K. Jain, "Tricontrollable pixelated metasurface for stopband for terahertz radiation," J. Electromag. Waves Appl. **34**(15), 2065–2078 (2020).
23. R. Agrahari, A. Lakhtakia, P. K. Jain, and S. Bhattacharyya, "Pixelated metasurfaces for linear-polarization conversion and absorption," J. Electromag. Waves Appl. **36**(7), 1008–1019 (2022).
24. M. Imada, A. Fujimori, and Y. Tokura, "Metal-insulator transitions," Rev. Mod. Phys. **70**(4), 1039–1263 (1998).
25. S. Cueff, J. John, Z. Zhang, J. Parra, J. Sun, R. Orobtchouk, S. Ramanathan, and P. Sanchis, "VO_2 nanophotonics," APL Photonics **5**(11), 110901 (2020).
26. K. Liu, S. Lee, S. Yang, O. Delaire, and J. Wu, "Recent progresses on physics and applications of vanadium dioxide," Mater. Today **21**(8), 875–896 (2018).
27. H. Lu, S. Clark, Y. Guo, and J. Robertson, "The metal–insulator phase change in vanadium dioxide and its applications," J. Appl. Phys. **129**(24), 240902 (2021).
28. R. Shi, N. Shen, J. Wang, W. Wang, A. Amini, N. Wang, and C. Cheng, "Recent advances in fabrication strategies, phase transition modulation, and advanced applications of vanadium dioxide," Appl. Phys. Rev. **6**(1), 011312 (2019).
29. F. J. Morin, "Oxides which show a metal-to-insulator transition at the Neel (*sic*) temperature," Phys. Rev. Lett. **3**(1), 34–36 (1959).

Optical Materials EXPRESS

30. D. Adler, "Mechanisms for metal-nonmental transitions in transition-metal oxides and sulfides," Rev. Mod. Phys. **40**(4), 714–736 (1968).
31. H. Kakiuchida, P. Jin, S. Nakao, and M. Tazawa, "Optical properties of vanadium dioxide film during semiconductive-metallic phase transition," Jpn. J. Appl. Phys. **46**(No. 5), L113–L116 (2007).
32. A. Lakhtakia, T. G. Mackay, and W. I. Waseer, "Thermal hysteresis in scattering by VO_2 spheres," J. Opt. Soc. Am. A **39**(10), 1921–1928 (2022).
33. A. M. Shaltout, V. M. Shalaev, and M. L. Brongersma, "Spatiotemporal light control with active metasurfaces," Science **364**(6441), eaat3100 (2019).
34. M. A. Kats, D. Sharma, J. Lin, P. Genevet, R. Blanchard, Z. Yang, M. M. Qazilbash, D. N. Basov, S. Ramanathan, and F. Capasso, "Ultra-thin perfect absorber employing a tunable phase change material," Appl. Phys. Lett. **101**(22), 221101 (2012).
35. M. Seo, J. Kyoung, H. Park, S. Koo, H.-S. Kim, H. Bernien, B. J. Kim, J. H. Choe, Y. H. Ahn, H.-T. Kim, N. Park, Q-H. Park, K. Ahn, and D.-s. Kim, "Active terahertz nanoantennas based on VO_2 phase transition," Nano Lett. **10**(6), 2064–2068 (2010).
36. H. Kocer, A. Ozer, S. Butun, K. Wang, J. Wu, H. Kurt, and K. Aydin, "Thermally tuning infrared light scattering using planar layered thin films and space gradient metasurface," IEEE J. Select. Topics Quantum Electron. **25**(3), 4700607 (2019).
37. V. Erçağlar, H. Hajian, A. E. Serebryannikov, and E. Ozbay, "Multifunctional tunable gradient metasurfaces for terahertz beam splitting and light absorption," Opt. Lett. **46**(16), 3953–3956 (2021).
38. T. T. Lv, Y. X. Li, H. F. Ma, Z. Zhu, Z. P. Li, C. Y. Guan, J. H. Shi, H. Zhang, and T. J. Cui, "Hybrid metamaterial switching for manipulating chirality based on VO_2 phase transition," Sci. Rep. **6**(1), 23186 (2016).
39. C. Zhang, G. Zhou, J. Wu, Y. Tang, Q. Wen, S. Li, J. Han, B. Jin, J. Chen, and P. Wu, "Active control of terahertz waves using vanadium-dioxide-embedded metamaterials," Phys. Rev. Appl. **11**(5), 054016 (2019).
40. M. Liu, Q. Xu, X. Chen, E. Plum, H. Li, X. Zhang, C. Zhang, C. Zou, J. Han, and W. Zhang, "Temperature-controlled asymmetric transmission of electromagnetic waves," Sci. Rep. **9**(1), 4097 (2019).
41. H. He, X. Shang, L. Xu, J. Zhao, W. Cai, J. Wang, C. Zhao, and L. Wang, "Thermally switchable bifunctional plasmonic metasurface for perfect absorption and polarization conversion based on VO_2," Opt. Express **28**(4), 4563–4570 (2020).
42. T. Lv, Y. Li, C. Qin, J. Qu, B. Lv, W. Li, Z. Zhu, Y. Li, C. Guan, and J. Shi, "Versatile polarization manipulation in vanadium dioxide-integrated terahertz metamaterial," Opt. Express **30**(4), 5439–5449 (2022).
43. J. Chen, X. Chen, K. Liu, S. Zhang, T. Cao, and Z. Tian, "A thermally switchable bifunctional metasurface for broadband polarization conversion and absorption based on phase-change material," Adv. Photonics Res. **3**(9), 2100369 (2022).
44. T. Paik, S.-H. Hong, E. A. Gaulding, H. Caglayan, T. R. Gordon, N. Engheta, C. R. Kagan, and C. B. Murray, "Solution-processed phase-change VO_2 metamaterials from colloidal vanadium oxide (VO_x) nanocrystals," ACS Nano **8**(1), 797–806 (2014).
45. A. E. Serebryannikov, K. B. Alici, E. Ozbay, and A. Lakhtakia, "Thermally sensitive scattering of terahertz waves by coated cylinders for tunable invisibility and masking," Opt. Express **26**(1), 1–14 (2018).
46. P. Kepič, F. Ligmajer, M. Hrtoň, H. Ren, L. de S.-Menezes, S. A. Maier, and T. Šikola, "Optically tunable Mie resonance VO_2 nanoantennas for metasurfaces in the visible," ACS Photonics **8**(4), 1048–1057 (2021).
47. A. E. Serebryannikov, A. Lakhtakia, M. Aalizadeh, E. Ozbay, and G. A. E. Vandenbosch, "Temperature-mediated invocation of the vacuum state for switchable ultrawide-angle and broadband deflection," Sci. Rep. **8**(1), 15044 (2018).
48. A. Tripathi, J. John, S. Kruk, Z. Zhang, H. S. Nguyen, L. Berguiga, P. R. Romeo, R. Orobtchouk, S. Ramanathan, Y. Kivshar, and S. Cueff, "Tunable Mie-resonant dielectric metasurfaces based on VO_2 phase-transition materials," ACS Photonics **8**(4), 1206–1213 (2021).
49. Q. Xing, C. Wang, S. Huang, T. Liu, Y. Xie, C. Song, F. Wang, X. Li, L. Zhou, and H. Yan, "Tunable graphene split-ring resonators," Phys. Rev. Appl. **13**(4), 041006 (2020).
50. W. Lai, R. Shi, H. Yuan, G. Liu, A. Amini, and C. Cheng, "Fully optically tunable and flexible composite films for enhanced terahertz control and multifunctional terahertz devices," ACS Appl. Electron. Mater. **3**(7), 3044–3051 (2021).
51. K. Dong, S. Hong, Y. Deng, H. Ma, J. Li, X. Wang, J. Yeo, L. Wang, S. Lou, K. B. Tom, K. Liu, Z. You, Y. Wei, C. P. Grigoropoulos, J. Yao, and J. Wu, "A lithography-free and field-programmable photonic metacanvas," Adv. Mater. **30**(5), 1703878 (2018).
52. H. Hajian, A. Ghobadi, A. E. Serebryannikov, B. Butun, G. A. E. Vandenbosch, and E. Ozbay, "VO_2-hBN-graphene-based bi-functional metamaterial for mid-infrared bi-tunable asymmetric transmission and nearly perfect resonant absorption," J. Opt. Soc. Am. B **36**(6), 1607–1615 (2019).
53. T. Wang, J. He, J. Guo, X. Wang, S. Feng, F. Kuhl, M. Becker, A. Polity, P. J. Klar, and Y. Zhang, "Thermally switchable terahertz wavefront metasurface modulators based on the insulator-to-metal transition of vanadium dioxide," Opt. Express **27**(15), 20347–20357 (2019).
54. A. E. Serebryannikov, A. Lakhtakia, G. A. E. Vandenbosch, and E. Ozbay, "Transmissive terahertz metasurfaces with vanadium dioxide split-rings and grids for switchable asymmetric polarization manipulation," Sci. Rep. **12**(1), 3518 (2022).

Optical Materials EXPRESS

55. J. Zhao, J. Song, T. Xu, T. Yang, and J. Zhou, "Controllable linear asymmetric transmission and perfect polarization conversion in a terahertz hybrid metal-graphene metasurface," Opt. Express **27**(7), 9773–9781 (2019).
56. S. V. Makarov, A. S. Zalogina, M. Tajik, D. A. Zuev, M. V. Rybin, A. A. Kuchmizhak, S. Juodkazis, and Y. Kivshar, "Light-induced tuning and reconfiguration of nanophotonic structures," Laser Photonics Rev. **11**(5), 1700108 (2017).
57. M. Taghinejad and W. Cai, "All-optical control of light in micro- and nanophotonics," ACS Photonics **6**(5), 1082–1093 (2019).
58. M. A. Motyka, B. D. Gauntt, M. W. Horn, and N. J. Podraza, "Microstructural evolution of thin film vanadium oxide prepared by pulsed-dc magnetron sputtering," J. Appl. Phys. **112**(9), 093504 (2012).
59. H. A. Basantani, S. Kozlowski, M.-Y. Lee, J. Li, S. S. N. Bharadwaja, E. C. Dickey, T. N. Jackson, and M. W. Horn, "Enhanced electrical and noise properties of nanocomposite vanadium oxide thin films by reactive pulsed-dc magnetron sputtering," Appl. Phys. Lett. **100**(26), 262108 (2012).
60. G. Subramanyam, E. Shin, P. R. Peri, R. Katiyar, G. Nazaripour, and S. Dey, "Structural, electrical, and electromagnetic properties of nanostructure vanadium dioxide thin films," in: G. Subramanyam, P. P. Banerjee, K. S. Gudmundsson, and A. Lakhtakia (eds.), *Thin Film Nanophotonics* (Elsevier, 2021).
61. CST Studio Suite (accessed 15 October 2022).
62. T. G. Mackay and A. Lakhtakia, *Electromagnetic Anisotropy and Bianisotropy: A Field Guide* (World Scientific, 2019).
63. M. J. Dicken, K. Aydin, I. M. Pryce, L. A. Sweatlock, E. M. Boyd, S. Walavalkar, J. Ma, and H. A. Atwater, "Frequency tunable near-infrared metamaterials based on VO_2 phase transition," Opt. Express **17**(20), 18330–18339 (2009).
64. M. A. Ordal, R. J. Bell, R. W. Alexander, L. L. Long, and M. R. Querry, "Optical properties of fourteen metals in the infrared and far infrared: Al, Co, Cu, Au, Fe, Pb, Mo, Ni, Pd, Pt, Ag, Ti, V, and W," Appl. Opt. **24**(24), 4493–4499 (1985).